Computers in Biology and Medicine 109 (2019) 207–217

Contents lists available at ScienceDirect

Computers in Biology and Medicine

journal homepage: www.elsevier.com/locate/compbiomed

IVUS images segmentation using spatial fuzzy clustering and hierarchical level set evolution

Menghua Xia[a], Wenjun Yan[a], Yi Huang[a], Yi Guo[a,b], Guohui Zhou[a,b], Yuanyuan Wang[a,b,*]

[a] Department of Electronic Engineering, Fudan University, Shanghai, 200433, China
[b] Key Laboratory of Medical Imaging Computing and Computer Assisted Intervention of Shanghai, Fudan University, Shanghai, 200433, China

ARTICLE INFO

Keywords:
Intravascular ultrasound
Border detection
Spatial fuzzy clustering
Hierarchical level set evolution

ABSTRACT

The detection of the lumen and media-adventitia (MA) borders in intravascular ultrasound (IVUS) images is crucial for quantifying plaque burdens. The challenge of the segmentation work mainly roots in various artifacts in the image. Most of the published methods involve the establishment of complex models but do not behave well on images with artifacts. In this study, aiming at automatically delineating borders in IVUS frames acquired by 20 MHz ultrasound probes, we present a fuzzy clustering-initialized hierarchical level set evolution (FC-HLSE) method. A cluster selection strategy based on the spatial fuzzy c-means (FCM) is proposed to generate the initial value and regularization term of the level set evolution (LSE). The contour convergence splits into two LSE steps between which an ingenious contour extraction (consisting of the morphological processing, the seek and linear interpolation, the gradient-based and circular fitting-based refinement) is carried out. We evaluate the proposed methodology on the publicly available 435 images by comparing auto-segmented results with the ground truth. The performance of the method is quantified using the Jaccard measure (JM), the Hausdorff distance (HD), the percentage of area difference (PAD), the linear regression and Bland-Altman analysis. Results reveal that our method can handle images with or without artifacts. The algorithm is able to extract the lumen/MA border with the JM of 0.90/0.89, the HD of 0.31/0.40 mm, the PAD of 0.07/0.08 in average, which is better in some cases compared with several state-of-the-art methods.

1. Introduction

Coronary atherosclerosis is the major cause of fatal cardiovascular diseases because of stenosis, failures in the proper treatment of plaques, and etc. [1]. Intravascular ultrasound (IVUS) is a catheter-based medical imaging modality capable of providing high-resolution and cross-sectional images of coronary arteries in real time. This technique enables the collection of the morphological and pathological information about the vessel [2]. The detection of the lumen border and the media-adventitia (MA) border is required to quantify the extent of stenosis and evaluate atherosclerotic plaque burdens. The manual segmentation is laborious and has to be operated by clinical experts. In addition, it is heavily affected by human subjectivity or uncertainty. The automatic border detection has been widely explored but has no standard solution, because of the presence of intravascular complicated structures (fibrotic plaque, calcification, and etc.), inherent artifacts (shadow artifacts, bifurcations, and etc.) and speckle noises [3]. This fact motivates us to develop the segmentation technique robust to various disturbances.

Attracted by intrinsic challenges of the IVUS images segmentation, many researchers attempt to extract boundaries using miscellaneous approaches, classified under deformable model-based methods [4–13], statistical and probabilistic methods [14–18], deep learning methods [19,20], as well as other methods [21–23]. Deformable model-based methods heavily depend on the extraction of the initial contour. Many techniques have been introduced to achieve the initial estimation, for example, the patch-based classification in the sparse representation framework [4], the pixel classification with an embedded feature selection technique [5], the texture-based classification [6], and the local binary pattern-based mask approach [7]. The influence of different feature descriptors in the segmentation process has been evaluated in Ref. [8]. Ref. [9,10] has proposed a 3D helical active contour evolving based on the Raleigh distribution of gray levels to detect the lumen border. Fast marching methods have also been applied to the IVUS images segmentation [11–13]. Statistically driven methods generally relate to the establishment of parametric or nonparametric models, for instance, a border search theory estimating the radial threshold [14], minimization of a cost function formulated using a probabilistic

* Corresponding author. Department of Electronic Engineering, Fudan University, Shanghai, 200433, China.
E-mail address: yywang@fudan.edu.cn (Y. Wang).

https://doi.org/10.1016/j.compbiomed.2019.04.029
Received 3 March 2019; Received in revised form 22 April 2019; Accepted 22 April 2019

approach [15], a holistic interpretation of the segmentation [16], a node-weighted directed graph with embedded shape constraints [17], and the Markov random field (MRF) into which the textural and edge information is integrated [18]. Deep learning is an active research area in the images segmentation lately. Ref. [19] has proposed the binary classification by two artificial neural networks (ANNs) to initialize the active contour. Ref. [20] has put forward a fully convolutional network architecture (IVUS-net) for the border detection. Among other categories of methods, the detection of boundaries has been released to the selection of extremal regions of extremum levels with a limitation that the shape of the contour is constrained to an epsilon [21]. Conventional integrated processes have also been investigated, such as the region-growing and unsupervised clustering methods [22], the mathematical morphology and convex hull techniques [23]. Ref. [2] has provided a review on segmentation algorithms in IVUS images.

As we can see, deformable model-based approaches usually initialize the active contour by using classifiers into which extracted and selected features are fed [4–6,19]. This sort of the initial estimation has at least one limitation, the need for annotated data and time consumption to train the classifier. Among the published methods, some are only applied to the MA border delineation [4,6,15], while some are only applied to the lumen [9,10,15,24]. In addition, some approaches are not fully automatic which require manual labels in one frame of an IVUS sequence [6,7,15] or manual interventions [9,11,12], and some work only on images without artifacts [8,22].

In this present study, we propose a fully automatic fuzzy clustering-initialized hierarchical level set evolution (FC-HLSE) method. The initial estimation is achieved by a novel cluster selection strategy premised on the spatial fuzzy c-means (FCM), which is more time-saving and free from annotated data, in contrast to the classifier training. Moreover, an ingenious contour extraction is inserted into two level set evolution (LSE) steps, making the algorithm robust to artifacts. Our method permits the detection for both lumen border and MA border on IVUS images with or without artifacts.

The rest of this paper is organized as follows. Section 2 firstly presents the preliminaries of this paper and then explicates the proposed method. In Section 3, we illustrate the experiments and parameters setting. Next, we present segmentation results obtained with the algorithm as well as the quantitative and qualitative analysis. The external discussion of our method is given in Section 4, and Section 5 is the concluding remarks.

2. Method

2.1. Preliminaries

2.1.1. Spatial fuzzy clustering

The k-means algorithm seeks to portion N objects into K clusters based on their attributes. In the image segmentation, N equals to the number of pixels $N_x \cdot N_y$ (N_x and N_y are columns and rows of the image respectively), and the attribute of the pixel (x, y) is denoted by $\zeta(x, y)$ (intensity, color, and etc.). The FCM utilizes the membership function $u_k(x, y)$ to indicate the degree of membership between the pixel (x, y) and the k^{th} cluster [25]. The FCM algorithm is optimized by minimizing a pre-defined cost function J, expressed as:

$$min\ J = \sum_{x=1}^{N_x} \sum_{y=1}^{N_y} \sum_{k=1}^{K} u_k(x, y)^p ||\zeta(x, y) - v_k||^2$$

$$subject\ to \quad \sum_{k=1}^{K} u_k(x, y) = 1 \qquad 0 \le u_k(x, y) \le 1$$

where v_k is the centroid of the k^{th} cluster, p is a weighting exponent controlling the fuzziness of clustering ($p = 2$ in this paper).

Membership functions and cluster centroids are updated by:

$$u_k(x, y) = \frac{\sum_{l=1}^{K} ||\zeta(x, y) - v_l||^{\frac{2}{(p-1)}}}{||\zeta(x, y) - v_k||^{\frac{2}{(p-1)}}} \tag{2}$$

$$v_k = \frac{\sum_{x=1}^{N_x} \sum_{y=1}^{N_y} u_k(x, y)^p \zeta(x, y)}{\sum_{x=1}^{N_x} \sum_{y=1}^{N_y} u_k(x, y)^p} \tag{3}$$

The spatial FCM incorporates spatial restrictions into the FCM by replacing $u_k(x, y)$ with $u'_k(x, y)$ [25],

$$u_k^{'}(x, y) = \frac{u_k(x, y)^{q1} \left[\sum_{(x,y) \in N_{(x,y)}} u_k(x, y) \right]^{q2}}{\sum_{l=1}^{K} \left\{ u_l(x, y)^{q1} \left[\sum_{(x,y) \in N_{(x,y)}} u_k(x, y) \right]^{q2} \right\}} \tag{4}$$

where $q1$, $q2$ are two constants controlling the relative importance of membership function $u_k(x, y)$ and spatial function . $N_{(x,y)}$ denotes a local window centered around the pixel (x, y) ($q1 = q2 = 1$, and $N_{(x,y)}$ is a square sized 5-by-5 pixel in this paper).

2.1.2. Level set method

The LSE has been extensively applied to image segmentation problems. It represents the planar closed curve as the zero-level-set of the level set function (LSF) in a higher dimension [26], as expressed:

$$C = \{(x, y) | \phi(x, y) = 0\} \tag{5}$$

The LSF is denoted by ϕ, the contour is denoted by C, $\phi > 0$ and $\phi < 0$ correspond to Ω_{in} and Ω_{out} (the region inside and outside C) respectively. Some involved notations in the LSE are stated in Table 1.

LSE models can be categorized into edge-based models and region-based models. Edge-based models make the utmost of the edge information of images but may suffer to boundary leakage problems if image edges are weak. Region-based models can converge on edges without the significant gradient. The classical region-based model was proposed by Ref. [27], the energy function with respect to ϕ is formulated by:

$$\begin{aligned} \varepsilon(\phi) = \beta \cdot \left\{ \int_{\Omega} \delta(\phi) |\nabla \phi| dxdy \right\} + \nu \cdot \left\{ \int_{\Omega} H(\phi) dxdy \right\} \\ + \lambda_{in} \int_{\Omega} (I - c_{in})^2 H(\phi) dxdy + \lambda_{out} \int_{\Omega} (I - c_{out})^2 (1 - H(\phi)) dxdy \end{aligned} \tag{6}$$

where $\Omega = \Omega_{in} \cup \Omega_{out}$, $\int_{\Omega} \delta(\phi) |\nabla \phi| dxdy$ is the length of C, $\int_{\Omega} H(\phi) dxdy$ is the area of Ω_{in}, $\delta(\phi)$ is the Dirac delta function, $H(\phi)$ is the Heaviside function, c_{in} and c_{out} are two constants approximating average image intensities in Ω_{in} and Ω_{out} respectively, computed by:

$$c_{in} = \frac{\int_{\Omega} I(x, y) \cdot H(\phi(x, y)) dxdy}{\int_{\Omega} H(\phi(x, y)) dxdy} \tag{7}$$

Table 1
The list of notations used in the level set evolution.

Definition	Notation
The image	I
The level set function	ϕ
The planar contour	$C(\phi = 0)$
The region inside the contour	$\Omega_{in}(\phi > 0)$
The region outside the contour	$\Omega_{out}(\phi < 0)$
The Dirac delta function [28]	$\delta(\phi)$
The Heaviside function [28]	$H(\phi)$
A Gaussian kernel with a standard deviation	G_{σ}
Weighing parameters	$\mu,\ \beta,\ \nu,\ \lambda_{in}, \lambda_{out}$

$$c_{out} = \frac{\int_{\Omega} I(x,y)\cdot(1 - H(\phi(x,y)))dxdy}{\int_{\Omega}(1 - H(\phi(x,y)))dxdy} \tag{8}$$

The energy function Eq. (6) can be minimized by solving the following gradient flow:

$$\frac{\partial\phi}{\partial t} = -\frac{\partial\varepsilon(\phi)}{\partial\phi}$$

$$= \beta\cdot\left\{\delta(\phi)div\left(\frac{\nabla\phi}{|\nabla\phi|}\right)\right\}$$

$$- \nu\cdot\delta(\phi) + \{-\lambda_{in}(I - c_{in})^2 + \lambda_{out}(I - c_{out})^2\}\cdot\delta(\phi)$$

One of the classical edge-based models is the distance regularized level set evolution (DRLSE) proposed by Ref. [28], implemented as:

$$\varepsilon(\phi) = \mu\cdot\left\{\frac{1}{2}\int_{\Omega}(|\nabla\phi| - 1)^2 dxdy\right\}$$

$$+ \beta\cdot\left\{\int_{\Omega} g\delta(\phi)|\nabla\phi|dxdy\right\} + \nu\cdot\left\{\int_{\Omega} gH(\phi)dxdy\right\} \tag{10}$$

The LSF is updated iteratively by:

$$\frac{\partial\phi}{\partial t} = -\frac{\partial\varepsilon(\phi)}{\partial\phi}$$

$$= \mu\cdot\left\{\Delta\phi - div\left(\frac{\nabla\phi}{|\nabla\phi|}\right)\right\}$$

$$+ \beta\cdot\left\{\delta(\phi)div\left(g\frac{\nabla\phi}{|\nabla\phi|}\right)\right\} - \nu\cdot g\delta(\phi) \tag{11}$$

where the first term is the distance regularization term eliminating the re-initialization in the evolution [28], the second term is a penalization of the weighted length of C, and the third term is a penalization of the weighted area of Ω_{in}. Δ is the Laplacian operator. g is the edge indicator which takes smaller values at image edges than at other locations, thereby slowing down the evolution of C at edges, formulated as:

$$g = \frac{1}{1 + |\nabla G_{\sigma} * I|^2} \tag{12}$$

2.2. Proposed method

Due to calcified plaques, bifurcations and other artifacts in IVUS images, vessel borders are not easily distinguished, which hinders the direct use of deformable models. The contour initialization and convergence are two essentials of deformable models. Hence, we adopt two different LSE equations to deform the contour in two steps for distinct purposes. The ingenious contour extraction and refinement are carried out between two LSEs, and the initial contour of the first round LSE is generated from the spatial FCM. The schematic of the method is depicted in Fig. 1.

2.2.1. Pre-processing and initialization

Firstly, we reduce speckle noises of ultrasound images using the nonlinear anisotropic diffusion filtering without removing significant parts of images, typically edges [29]. The parameter controlling the sensitivity to edges, the number of iterations and the parameter controlling speed of diffusion are fixed to 20, 3 and 0.2 respectively. The filtered image is denoted by I_f.

Employing the spatial FCM can identify approximate contours of the interest in a medical image. Assigning the intensity as the attribute in the clustering process ($\zeta(x,y) = I_f(x,y)$), we can get K images from which we select the one having the bright center point and the one having the smallest bright area to generate the initial estimation of the LSF for lumen and MA borders detection respectively, as shown in Fig. 1. The selected cluster is denoted by $I_{cluster}$.

We define the initial value of the LSF as [30]:

$$\phi(x,y,t=0) = 4([I_{cluster} \geq T_1] - 0.5) \tag{13}$$

2.2.2. The first round LSE

The first round LSE contributes to the robustness of the proposed method to plaques by separating interested regions from uninterested regions (separating the lumen and the adventitia from others for the lumen and MA borders detection respectively) in the evolution. In this regard, we adopt Eq. (14) amended from the region-based LSE equation proposed by Ref. [31]:

$$\frac{\partial\phi}{\partial t} = \mu\cdot\left\{\Delta\phi - div\left(\frac{\nabla\phi}{|\nabla\phi|}\right)\right\} + \beta\cdot\left\{\delta(\phi)div\left(g_{new}\frac{\nabla\phi}{|\nabla\phi|}\right)\right\}$$

$$+ \lambda\cdot\{[-(I - c_{in})^2 + (I - c_{out})^2]\cdot BF\cdot g_{new}\cdot\delta(\phi)\} \tag{14}$$

where $BF = 4\cdot I_{cluster}$, the third term is the balloon force driving the interface adaptively toward the object of interest. g_{new} is the object indicator expressed as [31]:

$$g_{new} = e^{-10\cdot\max\{\eta\cdot\hat{g},\ (1-\eta)\cdot\hat{g}_c\}} \tag{15}$$

where $\wedge$ denotes the unit normalization, and g_c is the edge indicator arisen from the selected cluster, formulated as:

$$g_c = \frac{1}{1 + |\nabla G_{\sigma} * I_{cluster}|^2} \tag{16}$$

We get the LSF ϕ_1 used for the following step after N_{iter} iterations.

2.2.3. Contour extraction and refinement

This section aims at getting the correct initialization of the second round LSE by employing operations illustrated below on the binarized image of ϕ_1. The lumen border detection takes steps 1), 2) and 3) in turn; the MA border detection takes steps 1), 2), 3), 4), and 3) successively. Specifically, the morphological processing alleviates the impact of plaques and noises to the algorithm, the linear interpolation contributes to the supplement of missing contour in bifurcations and shadow artifacts, the gradient-based refinement corrects the wrongly extracted contour caused by plaques, and the circular fitting-based refinement is for limiting the extracted contour approximated to the fitted circle (the shape of the MA border is similar to a circle generally). Examples of the contour extraction and refinement are shown in Fig. 2. The binary image determined by the extracted contour, denoted by I_{binary}, is used as the initial LSF in the second round LSE.

1) Morphological processing

For the lumen border detection, the white regions smaller than an empirically selected threshold T_{area} are deleted to get rid of small bright interferences inside the lumen border. Then a morphological close operation with a disk structuring element is executed. For the MA border detection, we find largest three connected areas L_1, L_2 and L_3. L_2 is considered to be part of the adventitia if its area is larger than the given threshold T_{area}, otherwise, it is deemed to be the plaque and is deleted (the area of the plaque is smaller than the area of the adventitia). L_3 is dealt with the same way.

2) Seek and linear interpolation

After converting the result of the step 1) to the polar coordinate system, we find the first edge point of each column, following by employing the linear interpolation for those columns having no edge points or edge points overstepping the range of $\mathscr{R}$ (distance in pixels from the center point of the image in the Cartesian space). Thus, points

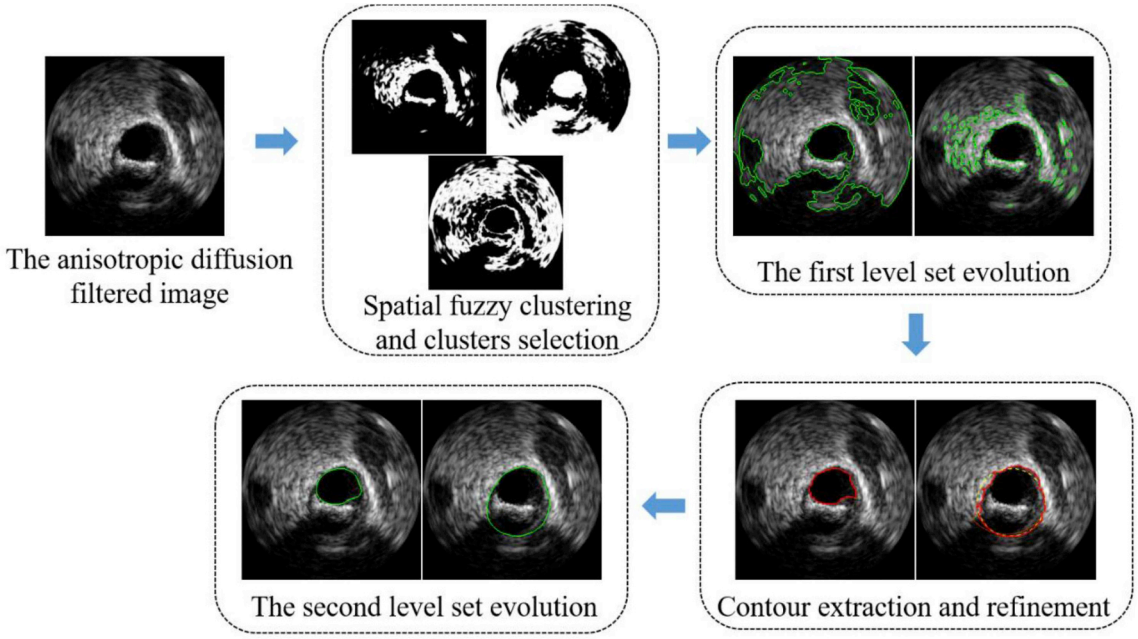

Fig. 1. The flowchart of the proposed methodology.

of the contour arise from either the seek or the linear interpolation.

3) Gradient-based refinement

By computing current curve's gradients to find points whose gradients are larger than a given threshold T_{grad}, we deduce segments of the curve needed to be rectified. Then, these segments are deleted and the linear interpolation is performed again. Finally, the resulting curve is converted to the Cartesian space.

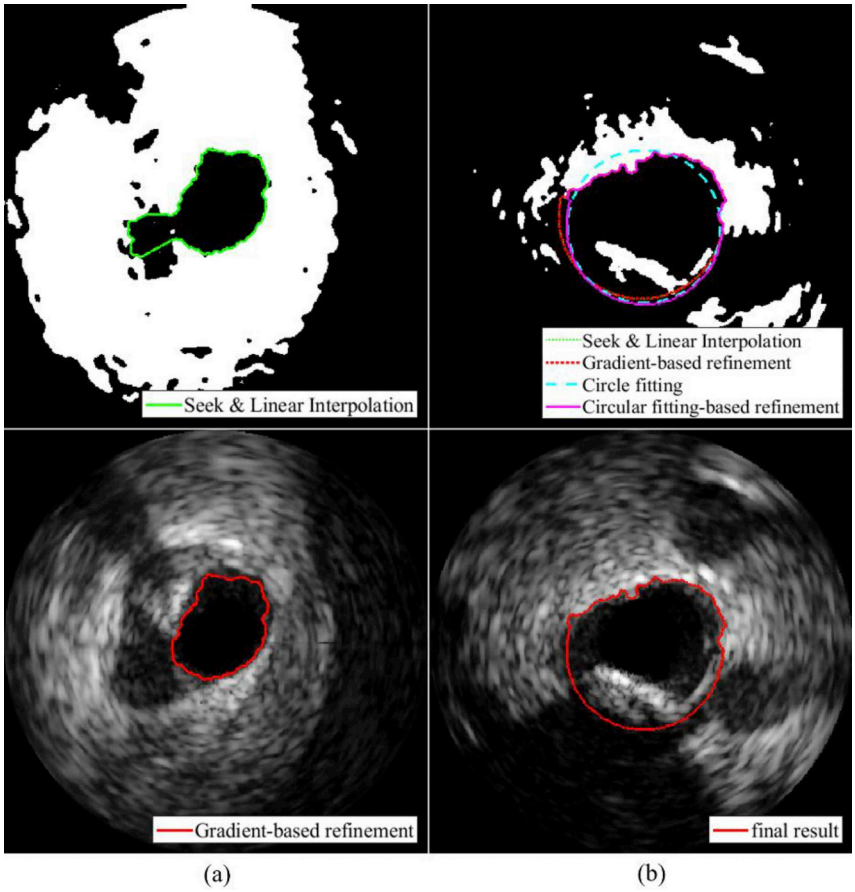

Fig. 2. Examples of the contour extraction and refinement for (a) the lumen border detection and (b) the media-adventitia border detection.

4) Circular fitting-based refinement

The current contour is fitted by a circle [32], then contour points supplemented through the linear interpolation are replaced by their corresponding circle-fitted points, and each point originating from the seek is similarly replaced by its corresponding circle-fitted point if the distance exceeds an empirically given value T_{dis}.

2.2.4. The second round LSE

In the second round LSE, targeting at converging the contour initialized by I_{binary} to vessel boundaries as closely as possible, we utilized the DRLSE of Eq. (11) to obtain final results after N_{iter} iterations.

Note that the discretization of Eq. (11) and Eq. (14) is implemented by approximating $\phi(t, x, y)$ to $\phi(n\tau, ih, jh)$ in the paper, expressed as:

$$\frac{\partial\phi(t,x,y)}{\partial t} = \frac{\phi(n\tau, ih, jh) - \phi(n\tau - \tau, ih, jh)}{\tau} = \frac{\phi_{i,j}^{n} - \phi_{i,j}^{n-1}}{\tau} \tag{17}$$

where τ is the time step, $h = 1$ is the space step, and n is the current iteration number ($n = 1,2, \cdots, N_{iter}$). i and j are the column and row numbers of the image respectively ($i = 1,2, \cdots, N_x$; $j = 1,2, \cdots, N_y$).

The gradient, Laplacian and divergence operators are discretized by:

$$\nabla\phi_{i,j} = (\nabla^x\phi_{i,j}, \nabla^y\phi_{i,j}) = \left(\frac{\phi_{i+1,j} - \phi_{i-1,j}}{2}, \frac{\phi_{i,j+1} - \phi_{i,j-1}}{2}\right) \tag{18}$$

$$\Delta\phi_{i,j} = \phi_{i+1,j} + \phi_{i-1,j} + \phi_{i,j+1} + \phi_{i,j-1} - 4\cdot\phi_{i,j} \tag{19}$$

$$div\left(\frac{\nabla\phi_{i,j}}{|\nabla\phi_{i,j}|}\right) = \nabla^x\left(\frac{\nabla^x\phi_{i,j}}{\sqrt{(\nabla^x\phi_{i,j})^2 + (\nabla^y\phi_{i,j})^2}}\right) + \nabla^y\left(\frac{\nabla^y\phi_{i,j}}{\sqrt{(\nabla^x\phi_{i,j})^2 + (\nabla^y\phi_{i,j})^2}}\right) \tag{20}$$

3. Experiments and results

3.1. Materials and experiments

The experimental evaluation of our method is conducted on the publicly available dataset provided by Ref. [3]. We adopt the dataset B which consists of 435 images from 10 patients using a Si5 (Volcano Corporation) with a 20 MHz Eagle Eye monorail catheter. The adopted dataset covers various complex situations, which makes the border extraction more demanding. Specifically, the dataset includes 60 images containing bifurcations, 94 images suffering from side vessel artifacts, and 106 images with shadow artifacts (some images contain multiple artifacts). There are also 225 images containing no distinct artifacts other than plaques. Considering the sophistication and multiplicity of images in the dataset, three sets of manual delineations drawn by two clinical experts, denoted by Obs1 (the view of observer 1), Obs2v1 (the first view of observer 2) and Obs2v2 (the second view of observer 2), have been provided as the ground truth [3].

The algorithm is implemented on a Dell Inc Precision T7610 with Intel (R) Xeon(R) CPU E5-2637 v2, 3.5 GHz, 64 GB RAM, with Matlab R2018a on Windows 10.

The self-evaluation and the comparative evaluation are carried out to assess the proposed method. First, self-evaluation is performed on the FC-HLSE, FC-LSE1 (without the 2^{nd} round LSE), and FC-LSE2 (without the 1^{st} round LSE) to prove the capability of the method to segment IVUS images, as well as validating the effectiveness of the hierarchical mechanism. Intra- and inter-observer evaluations are also employed to quantify the ground truth uncertainty. Second, in order to appraise the proposed method more objectively, we draw a fair comparison between the FC-HLSE and nine other methods conducted on the same dataset (comparative evaluation).

3.2. Evaluation measures

The widely utilized quantitative performance analysis of the auto-segmented result against the ground truth in IVUS images can be mainly grouped into two categories: the boundary-based evaluation metrics and the region-based evaluation metrics. Three different indicators [3] are used in this paper. The Hausdorff distance (HD) is utilized as the boundary-based metric, while the Jaccard measure (JM) and the percentage of area difference (PAD) are utilized as region-based evaluation metrics. Smaller HD and PAD are preferred while larger JM is preferred.

The HD between the auto-segmented contour (C_{auto}) and the ground truth (C_{truth}) is the maximum distance of the point on C_{auto} to the nearest point on C_{truth}, defined as:

$$HD = \max_{a\in C_{auto}}\left\{\min_{b\in C_{truth}}\{D(a,b)\}\right\} \tag{21}$$

where $D(a, b)$ is the Euclidean distance between points a and b.

The JM quantifies the overlapping area between automatic and manual segmentation results as computed by the following equation:

$$JM = \frac{|R_{auto} \cap R_{truth}|}{|R_{auto} \cup R_{truth}|} \tag{22}$$

where R_{auto} is the vessel region segmented automatically and R_{truth} represents the region segmented by the ground truth.

The PAD calculates the segmentation area difference between R_{auto} and R_{truth}, computed as:

$$PAD = \frac{|Area_{auto} - Area_{truth}|}{Area_{truth}} \tag{23}$$

In addition, the linear regression is used to compare areas inside the automatic border and inside the manual border quantitatively. Further, the Bland-Altman plot known as scatter plots of the difference against the mean between two measurements is utilized to visualize the potential bias and errors in the border detection.

3.3. Parameters selection

Parameters involved in the FC-HLSE is essential for results. Table 2 displays descriptions and values of parameters in the algorithm. Details about the setting of parameters are illustrated below. Values selected are maintained the same during the border extraction process.

In the spatial FCM initialization process, the number of clusters K is set to 3 in which clustering results match different tissues best, as shown in Fig. 3.

In the step of contour extraction and refinement, thresholds are empirically chosen according to features of images, in the purpose of hampering the influence of artifacts. In the binarization process illustrated in Eq. (13), T_1 is set to 0.8, below which pixels (having a weak membership with the cluster centroid and usually being undesirable disturbances) are blackened. Since the area of the interference (or the plaque) inside the lumen border (or the MA border) is usually less than 540 $pixel^2$ (or 2700 $pixel^2$), T_{area} is set to 540 $pixel^2$ (or 2700 $pixel^2$). As for $\mathscr{R}$, the fact that the border usually locates within a certain range from the image center facilitates its value selection.

In the LSE, parameters controlling the evolution and shape of the contour are determined through tunning. Specifically, a larger time step τ allows a faster evolution, but the product of μ and τ should be less than 0.25 to ensure the stabilization of the curve evolution (usually $\mu\cdot\tau = 0.2$ [28]). We assign $\tau = 1$ and $\mu = 0.2$. The larger value the β takes, the smoother the contour is. The MA border usually has an approximated circular form while the lumen border has an irregular shape, thus β takes the value of 1 and 7 in the 2^{nd} round LSE for the lumen and MA borders respectively. The sign of ν determines the propagation direction of the contour (positive for expansion and negative

Table 2
Parameters setting in the proposed method.

Step	Variable	Definition	Value	
Pre-processing and initialization	K	The number of clusters in the spatial fuzzy c-means	3	
	T_1	A threshold in the initialization of the level set function (Eq. (13))	0.8	
Contour extraction and refinement	T_{area}	An area threshold in the morphological processing	540 $pixel^2$(lumen)/2700 $pixel^2$(MA)	
	$\mathscr{R}$	The range of distance in pixels in the seek and linear interpolation	[28,137](lumen)/[31,180](MA)	
	T_{grad}	A gradient threshold in the gradient-based refinement	5(lumen)/7(MA)	
	T_{dis}	A distance threshold in the circular fitting-based refinement	57 pixel	
			the 1^{st} round	**the 2^{nd} round**
Level set evolution	μ	Weighting coefficient of the distance regularization term	0.2	
	σ	The standard deviation of the Gaussian kernel	0.7	
	ε	Regulator for $\delta(\phi)$	1	
	τ	Time step of the level set evolution	1	
	β	Weighting coefficient of the length penalization term	3	1(lumen)/7(MA)
	λ	Weighting coefficient of the balloon force (Eq. (14))	−0.03	/
	ν	Weighting coefficient of the area penalization term (Eq. (11))	/	0.03
	η	Parameter balancing the contributions of different object indicators (Eq. (15))	0.5	/
	N_{iter}	The number of iterations	40(lumen)/10(MA)	80

for shrinkage), the ideal ν takes a value close to zero around the target border but a large value on other regions [26]. As the initial contour is close to and inside the target border in the 2^{nd} round LSE as illustrated in Fig. 2, we assign ν the value of 0.03. When the performance of the algorithm increases not obviously or decreases with increasing N_{iter}, we consider the contour has converged to the vessel boundary. As illustrated in Fig. 4, when N_{iter} increases up to 40/80 and 10/80 (the 1^{st}/2^{nd} round LSE) for the lumen and MA respectively, the algorithm is nearly optimized.

3.4. Results

3.4.1. Self-evaluation of the border detection

Results of the proposed FC-HLSE, FC-LSE1 and FC-LSE2 by comparing auto-segmented results with the ground truth, as well as intra- and inter-observer evaluations are listed in Table 3. Cumulative distributions of the HD and PAD are plotted in Fig. 5. The JM of 0.90 ± 0.05, the HD of 0.29 ± 0.21 mm and the PAD of 0.06 ± 0.06 are achieved for the lumen border while the JM of 0.88 ± 0.11, the HD of 0.43 ± 0.36 mm and the PAD of 0.10 ± 0.13 are achieved for the MA border. Resulting metrics are close to intra- and inter-observer variabilities as shown in Fig. 5, which could demonstrate the capability of the proposed method for the IVUS images segmentation.

In addition, the FC-HLSE outperforms FC-LSE1 and FC-LSE2, illustrating that each step of the hierarchical LSE could improve the border detection. The 1^{st} LSE yields the mean improvement of 0.03, 0.10 mm and 0.03 in the JM, HD, and PAD respectively for the lumen border detection while 0.01, 0.13 mm and 0 in the JM, HD and PAD respectively for the MA border detection. The corresponding values raised by the 2^{nd} LSE are 0.02, 0.03 mm, 0.03, 0.01, 0.01 mm and 0 respectively.

Further, the linear regression as shown in Fig. 6 reports a good agreement and a high correlation (> 0.95 and > 0.89 for the lumen and MA respectively) between areas inside automatically extracted borders and experts defined contours. The mean value of the difference (bias) in the Bland-Altman plot (Fig. 7 (a,d)) is relatively close to 0 compared with the inter-observer (Fig. 7 (b,e)) and intra-observer (Fig. 7 (c,f)) variabilities, indicating the accuracy and consistency of the proposed segmentation method.

Furthermore, examples of automatically detected lumen and MA borders along with manual drawings on frames with various artifacts are displayed in Fig. 8, showing that our algorithm has satisfactory outcomes even for low-quality images contaminated by bifurcations, side vessel artifacts, plaques, and shadow artifacts.

3.4.2. Comparative evaluation with other methods

Quantitative comparative results with previous methods during recent years are summarized in Table 4, covering categories of artifacts. The empty cell in the table means that researchers have not implemented their method for that specific category of data. The proposed FC-HLSE has better results in some cases especially for the MA border detection. In particular, our approach yields the largest JM in almost all cases.

4. Discussion

In this paper, we present the FC-HLSE method for the IVUS images segmentation. Next, we discuss the method from three aspects: the choice of LSE models, the detailed analysis of results and the assessment of advantages and weaknesses, illustrated in the following paragraphs.

The success of the proposed method depends heavily on the cooperation of the deformable model and the contour extraction. The evolution of the active contour (including the parametric active contour

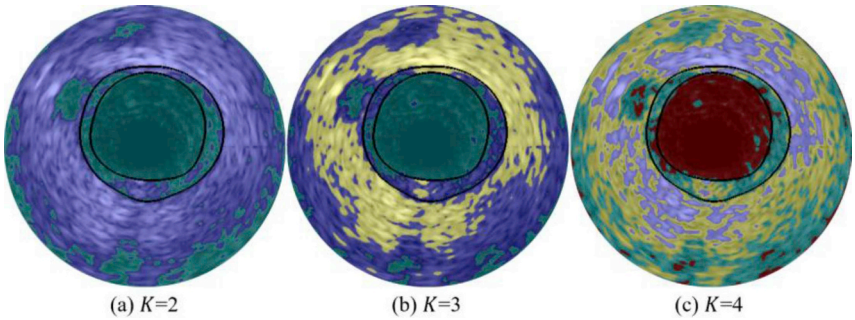

Fig. 3. Spatial fuzzy c-means clustering results. Different clusters are imposed with different colors. The black contour is the ground truth of the lumen and MA borders.

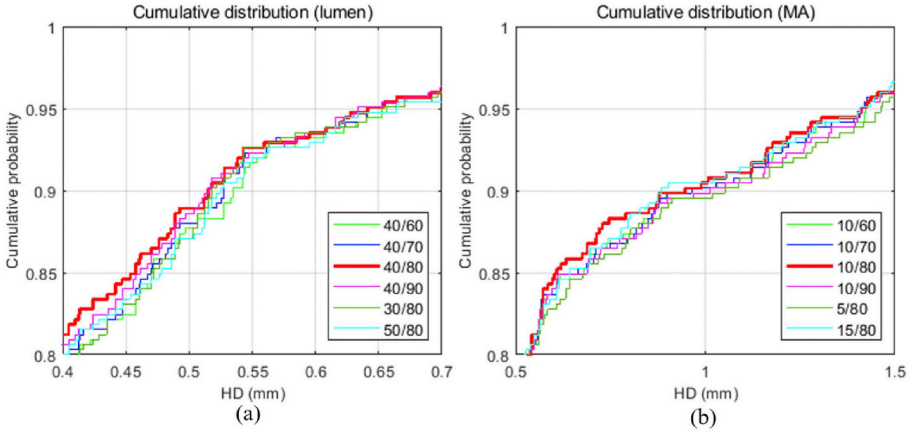

Fig. 4. Crops of the cumulative distribution of HD between auto-segmented results and the ground truth when the number of iterations for the $1^{st}/2^{nd}$ LSE take different values.

and the geometric active contour) is easily controlled by tuning parameters and adding restrictions to the evolution equation. In addition, it is easy for the geometric active contour (LSF) to follow shapes that change topologically. Thus, two different LSE models are selected for distinct purposes. The 1^{st} round LSE is for separating interested regions from uninterested regions. According to our tests, the improved region-based LSE of Eq. (14) achieves the best result among several LSE models. Usually, through the spatial FCM and the 1^{st} round LSE, plaques could depart the adventitia as displayed in Fig. 9(a). However, in some particular circumstances, the departure could not be achieved, which leads to the wrong detection as shown in Fig. 9(b). The 2^{nd} round LSE is for driving the contour to the ideal location. Because the current initial contour is relatively near to the ideal border, so it would be preferable to adopt the edge-based LSE of Eq. (11) making the best of edge information of images.

The major advantage of the FC-HLSE lies in its robustness to image artifacts (Fig. 8). As shown in Table 3, the method has admirable results (average 0.91 and 0.92 in the JM, 0.06 and 0.05 in the PAD, 0.27 mm and 0.30 mm in the HD for the lumen and MA respectively) in IVUS images without artifacts and satisfying results in images with multiple artifacts. There are 19 outliers in Fig. 7 (a) of the lumen border detection, of which numbers of frames belonging to the category of no artifact, bifurcation, side vessels, and shadow are 3, 8, 5, and 4 respectively. There are 22 outliers in Fig. 7 (d) of the MA border detection, of which numbers of frames belonging to the category of no artifact, bifurcation, side vessels, and shadow are 1, 8, 10, and 14 respectively. It is worth mentioning that results in terms of the boundary-based evaluation metric (HD) are not so good as results in terms of the region-based evaluation metric (JM and PAD). We believe that the high HD comes from two aspects: one is the incorrect contour extraction in some cases as shown in Fig. 9(b), the other is the grayscale inhomogeneity impeding the contour convergence towards the target boundary.

Table 4 indicates the comparison with the other nine methods. The proposed FC-HLSE achieves best results for the MA border detection in all cases except the HD of the no artifact category (the IVUS-net [20]

Table 3
The performance of the proposed method on the testing set (326 frames) of publicly available dataset [3]. Measures represent the mean and standard deviation computed according to the ground truth.

		Lumen			MA		
		HD	JM	PAD	HD	JM	PAD
General performance	**FC-HLSE**	**0.29 (0.21)**	**0.90 (0.05)**	**0.06 (0.06)**	**0.43 (0.36)**	**0.88 (0.11)**	**0.10 (0.13)**
	FC-LSE1	0.39 (0.22)	0.87 (0.05)	0.09 (0.06)	0.56 (0.38)	0.87 (0.11)	0.10 (0.13)
	FC-LSE2	0.32 (0.21)	0.88 (0.06)	0.09 (0.06)	0.44 (0.36)	0.87 (0.11)	0.10 (0.13)
	intra-observer	0.17 (0.13)	0.93 (0.05)	0.04 (0.06)	0.14 (0.10)	0.95 (0.04)	0.03 (0.03)
	inter-observer	0.28 (0.13)	0.88 (0.05)	0.11 (0.08)	0.24 (0.12)	0.93 (0.03)	0.06 (0.04)
No artifact	**FC-HLSE**	**0.27 (0.16)**	**0.91 (0.04)**	**0.06 (0.05)**	**0.30 (0.18)**	**0.92 (0.05)**	**0.05 (0.05)**
	FC-LSE1	0.38 (0.19)	0.88 (0.04)	0.08 (0.05)	0.44 (0.22)	0.92 (0.05)	0.05 (0.05)
	FC-LSE2	0.31 (0.20)	0.89 (0.06)	0.09 (0.06)	0.30 (0.18)	0.92 (0.05)	0.05 (0.06)
	intra-observer	0.15 (0.11)	0.94 (0.05)	0.04 (0.04)	0.12 (0.08)	0.96 (0.03)	0.02 (0.03)
	inter-observer	0.25 (0.12)	0.89 (0.04)	0.09 (0.06)	0.20 (0.07)	0.93 (0.02)	0.05 (0.03)
Bifurcation	**FC-HLSE**	**0.49 (0.33)**	**0.85 (0.08)**	**0.09 (0.09)**	**0.69 (0.44)**	**0.81 (0.14)**	**0.15 (0.18)**
	FC-LSE1	0.59 (0.33)	0.83 (0.08)	0.10 (0.09)	0.81 (0.47)	0.80 (0.14)	0.17 (0.20)
	FC-LSE2	0.48 (0.29)	0.84 (0.07)	0.10 (0.08)	0.69 (0.44)	0.80 (0.14)	0.15 (0.20)
	intra-observer	0.25 (0.23)	0.90 (0.08)	0.07 (0.11)	0.18 (0.12)	0.94 (0.04)	0.04 (0.05)
	inter-observer	0.38 (0.17)	0.84 (0.07)	0.16 (0.12)	0.33 (0.21)	0.90 (0.05)	0.08 (0.06)
Side vessels	**FC-HLSE**	**0.24 (0.13)**	**0.90 (0.04)**	**0.06 (0.04)**	**0.50 (0.45)**	**0.86 (0.12)**	**0.13 (0.17)**
	FC-LSE1	0.35 (0.19)	0.88 (0.04)	0.08 (0.05)	0.60 (0.49)	0.85 (0.12)	0.13 (0.19)
	FC-LSE2	0.26 (0.14)	0.89 (0.05)	0.08 (0.05)	0.51 (0.45)	0.85 (0.12)	0.13 (0.17)
	intra-observer	0.15 (0.08)	0.93 (0.04)	0.04 (0.04)	0.15 (0.10)	0.95 (0.04)	0.03 (0.04)
	inter-observer	0.27 (0.12)	0.87 (0.06)	0.13 (0.09)	0.22 (0.14)	0.92 (0.05)	0.06 (0.05)
Shadow	**FC-HLSE**	**0.28 (0.19)**	**0.88 (0.06)**	**0.07 (0.06)**	**0.62 (0.48)**	**0.80 (0.15)**	**0.17 (0.19)**
	FC-LSE1	0.37 (0.20)	0.86 (0.06)	0.10 (0.06)	0.72 (0.47)	0.80 (0.15)	0.17 (0.20)
	FC-LSE2	0.31 (0.19)	0.87 (0.06)	0.09 (0.07)	0.63 (0.48)	0.80 (0.15)	0.17 (0.20)
	intra-observer	0.15 (0.13)	0.92 (0.06)	0.04 (0.07)	0.17 (0.14)	0.94 (0.05)	0.04 (0.04)
	inter-observer	0.28 (0.14)	0.87 (0.06)	0.12 (0.09)	0.26 (0.14)	0.91 (0.04)	0.06 (0.05)

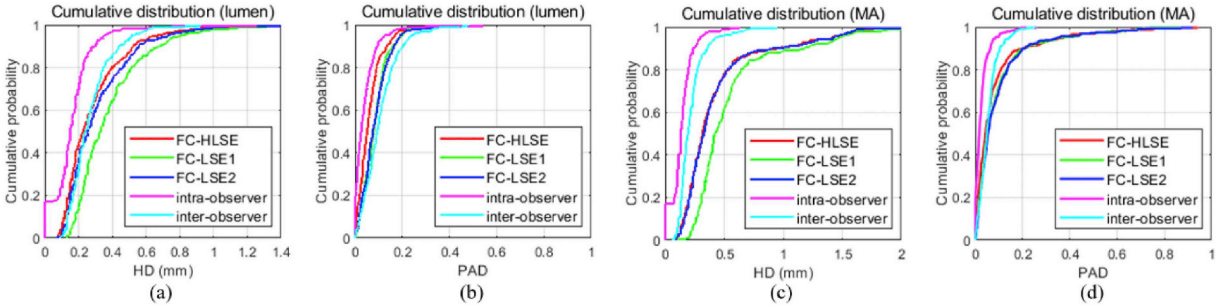

Fig. 5. Cumulative distribution of HD and PAD between auto-segmented results and the ground truth, along with intra- and inter-observer evaluations.

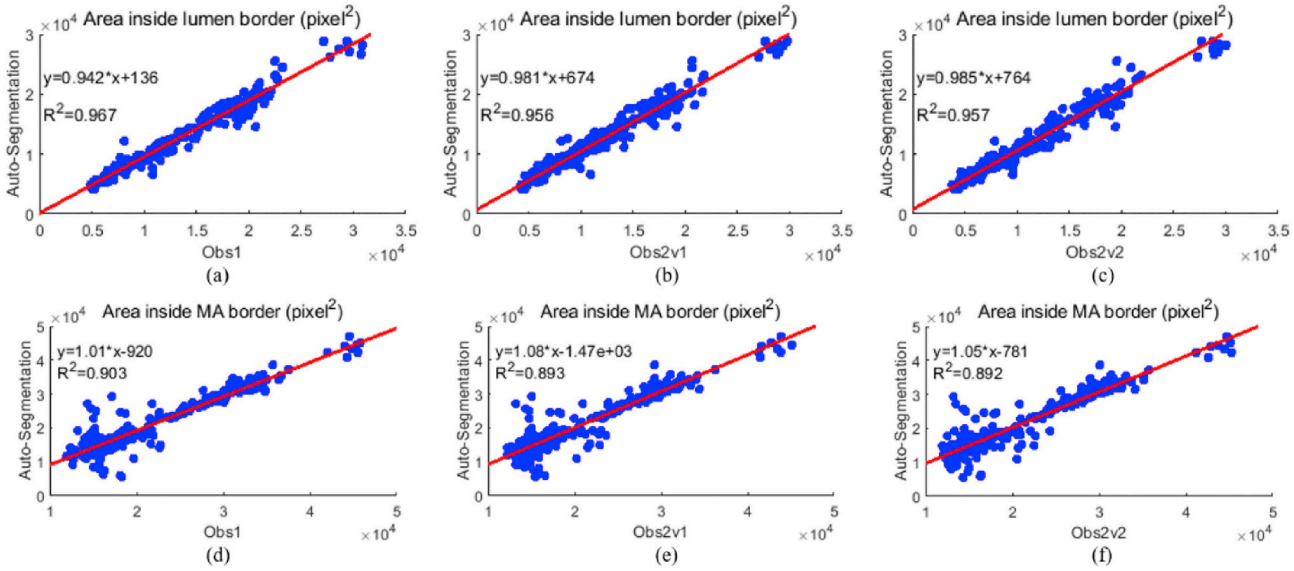

Fig. 6. The linear regression for the comparison of areas inside the lumen border (first row), the MA border (second row) detected by the proposed method and Obs1 (first column), Obs2v1 (second column) and Obs2v2 (third column).

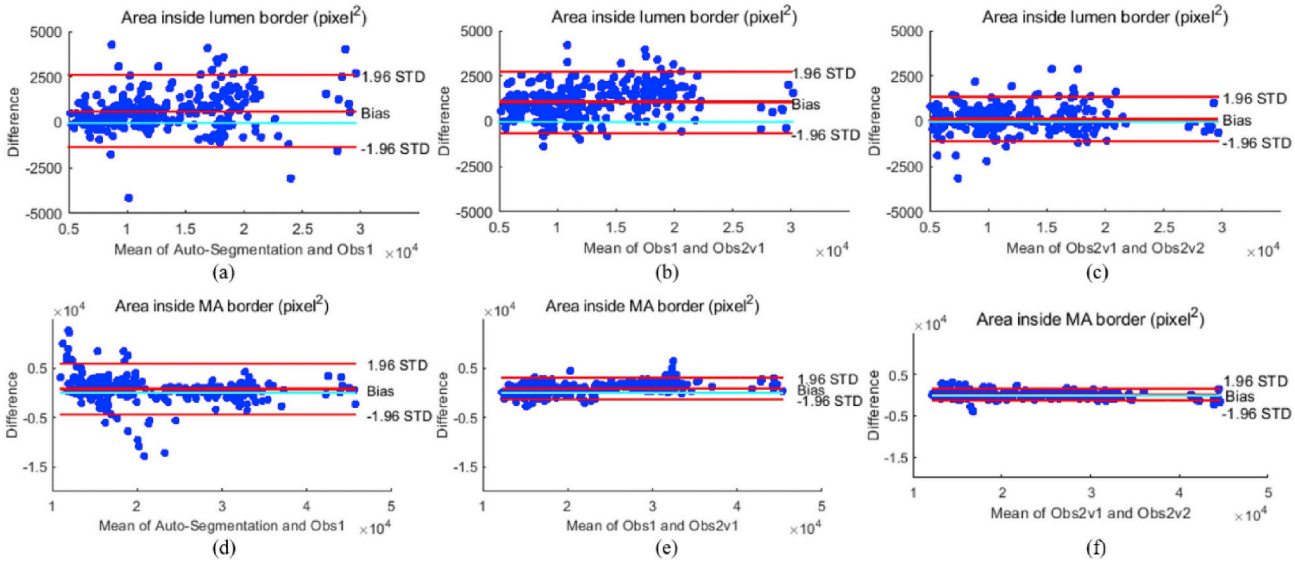

Fig. 7. Bland-Altman plots for the comparison of areas inside the lumen border (first row), the MA border (second row) detected by the proposed method and Obs1 (first column), Obs1 and Obs2v1 (second column), Obs2v1 and Obs2v2 (third column). The line of the zero difference is depicted in cyan.

performs best) and the PAD of the shadow category (the nonparametric statistical approach [14] does best). As for the lumen border detection, the FC-HLSE has superiority over other methods in cases not including the category of no artifact (only ranks after the IVUS-net) in terms of the JM. The performance of the FC-HLSE judged by the PAD is merely weaker than the 3D helix model [10]. The HDs of the FC-HLSE are smaller than most methods although the IVUS-net has the minimum values in general. Considering the time consumption per frame and

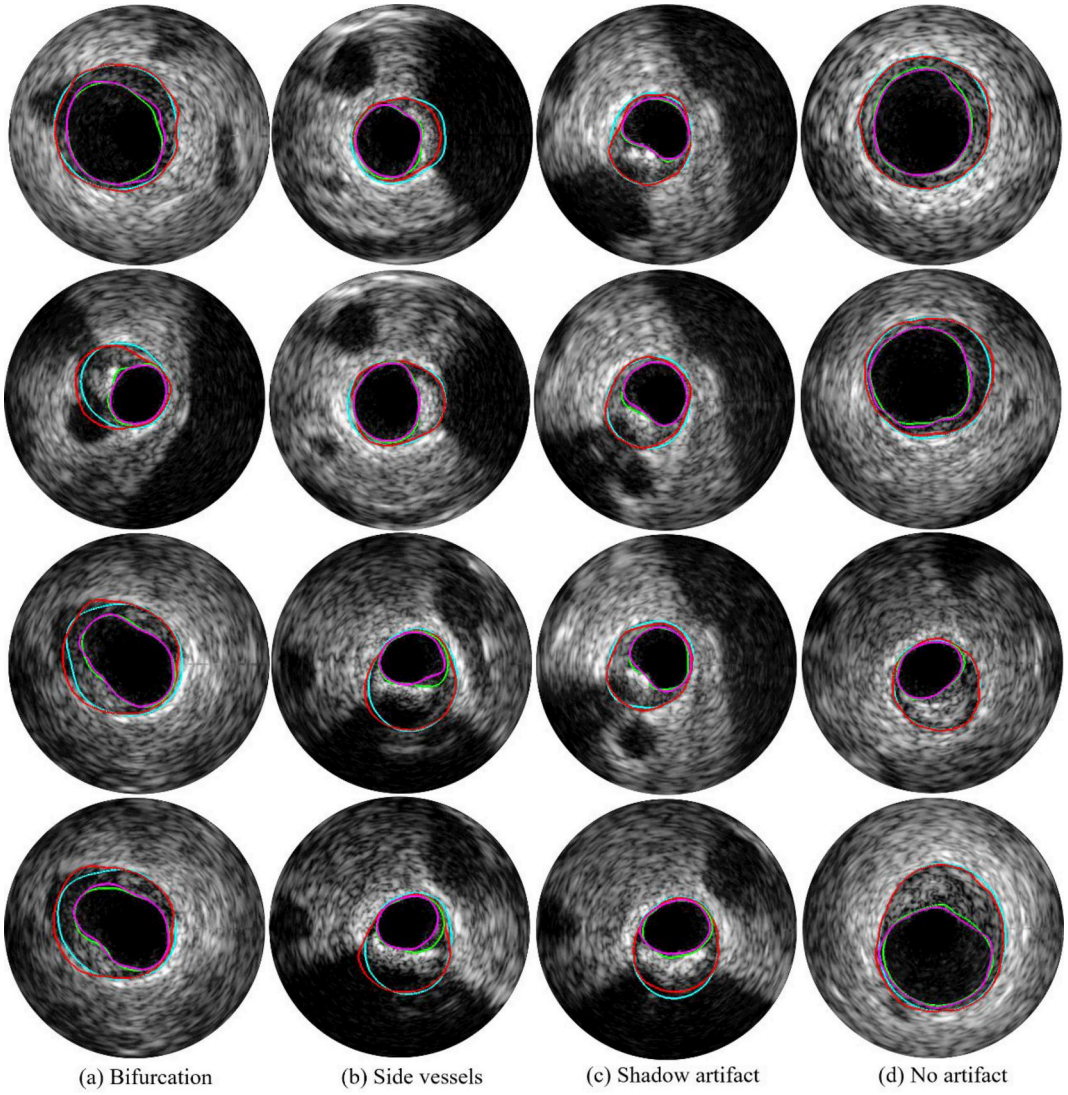

Fig. 8. Examples of segmentation results categorized under (a) bifurcation, (b) side vessels, (c) shadow artifact, and (d) no artifact. Most of the images have plaques. The green, cyan, magenta, and red contours correspond to the manually annotated lumen border, the manually annotated MA border, the auto-detected lumen border, and the auto-detected MA border respectively.

neglecting the computer dependence, the FC-HLSE has weakness compared with the IVUS-net and the 3D helix model as illustrated in Table 5. However, the IVUS-net requires much time to train the fully connected network.

Apart from the above, FC-HLSE offers several other advantages. The initialization of the deformable model is implemented by the spatial FCM, which requires no training for any classifiers (in contrast to some methods based on the pixel classification [4–6,19]. Further, the number of iterations can be decreased minorly to alleviate the computational burden in the clinical application.

5. Conclusion

Vessel boundaries detection is a hot topic in the IVUS images studying and analyzing. In this paper, we present the FC-HLSE strategy for the automatic lumen and MA borders detection in IVUS images. The segmented borders in 435 images from 10 patients are assessed to be accurate as indicated by quantified evaluations using three metrics, namely the JM, HD, and PAD. The small average HD of (0.31 ± 0.20) mm/(0.40 ± 0.34) mm, the small average PAD of (0.07 ± 0.06)/(0.08 ± 0.12), and the high average JM of (0.90 ± 0.05)/(0.89 ± 0.10) for the lumen/MA are achieved, indicating that the proposed segmentation algorithm is successful. The statistic results are also compared with other published IVUS images segmentation methods on the same dataset, which demonstrates that our method has admirable results on both non-artifact and artifact images. Since the dataset covers various pathological cases, the method could do well on the segmentation of 20 MHz IVUS frames. Our method can provide the quantified information for the clinical diagnosis and for the surgical guidance.

Further studies can be conducted for incorporating the texture information into the fuzzy clustering or LSE models to get more accurate results. In addition, it would be significative to generate the automatic parameters setting mechanism according to the IVUS image or sequence. The method has also been adapted for IVUS images acquired by 40 MHz probes (Boston Scientific) with the preliminary results unsatisfactory. We plan to investigate the simultaneous segmentation of 20 MHz and 40 MHz IVUS frames in our future work.

Conflicts of interest

None Declared.

Table 4
The statistical comparison with other methods on 435 frames of dataset B [3] for each individual category. Format is set as the mean value (the standard deviation). The best results are highlighted in bold.

		Lumen			MA		
		HD	JM	PAD	HD	JM	PAD
General performance	FC-HLSE	0.31 (0.20)	**0.90(0.05)**	0.07 (0.06)	**0.40(0.34)**	**0.89(0.10)**	**0.08(0.12)**
	Hammouche et al. [10]	0.27 (0.14)	0.89 (0.05)	**0.05(0.06)**	–	–	–
	Kermani et al. [14]	0.38 (0.26)	0.84 (0.07)	0.11 (0.08)	0.64 (0.41)	0.82 (0.11)	0.13 (0.11)
	Faraji et al. [21]	0.30 (0.20)	0.87 (0.06)	0.08 (0.09)	0.67 (0.54)	0.77 (0.17)	0.19 (0.18)
	Yang et al. [20]	**0.26(0.25)**	0.90 (0.06)	–	0.48 (0.44)	0.86 (0.11)	–
	Jodas et al. [24]	0.29 (0.17)	0.88 (0.06)	0.09 (0.07)	–	–	–
	Mendizabal et al. [15]	0.38 (0.26)	0.84 (0.08)	0.11 (0.12)	–	–	–
	Wang et al. [3]	0.51 (0.25)	0.83 (0.08)	0.14 (0.12)	–	–	–
	Alberti et al. [3]	0.46 (0.30)	0.79 (0.08)	0.16 (0.09)	–	–	–
No artifact	FC-HLSE	0.30 (0.17)	0.90 (0.04)	0.07 (0.05)	0.29 (0.17)	**0.93(0.05)**	**0.04(0.05)**
	Hammouche et al. [10]	0.26 (0.11)	0.90 (0.04)	**0.05(0.04)**	–	–	–
	Kermani et al. [14]	0.36 (0.21)	0.85 (0.07)	0.10 (0.08)	0.43 (0.23)	0.87 (0.05)	0.11 (0.06)
	Faraji et al. [21]	0.29 (0.17)	0.88 (0.05)	0.08 (0.07)	0.31 (0.23)	0.89 (0.07)	0.07 (0.08)
	Yang et al. [20]	**0.21(0.09)**	**0.91(0.03)**	–	**0.27(0.23)**	0.92 (0.05)	–
	Lo Vercio et al. [8]	–	0.83 (0.05)	0.18 (0.06)	–	0.85 (0.04)	0.15 (0.04)
Bifurcation	FC-HLSE	0.48 (0.29)	**0.86(0.07)**	0.09 (0.09)	**0.64(0.40)**	**0.84(0.13)**	**0.13(0.16)**
	Hammouche et al. [10]	**0.40(0.21)**	0.85 (0.07)	**0.08(0.10)**	–	–	–
	Kermani et al. [14]	0.47 (0.32)	0.83 (0.07)	0.12 (0.08)	0.99 (0.53)	0.74 (0.13)	0.22 (0.20)
	Faraji et al. [21]	0.53 (0.34)	0.79 (0.10)	0.15 (0.17)	1.22 (0.45)	0.57 (0.13)	0.32 (0.19)
	Yang et al. [20]	0.50 (0.58)	0.82 (0.11)	–	0.82 (0.60)	0.78 (0.11)	–
	Mendizabal et al. [15]	0.53 (0.36)	0.79 (0.12)	0.17 (0.18)	–	–	–
	Wang et al. [3]	0.54 (0.27)	0.81 (0.11)	0.14 (0.13)	–	–	–
	Alberti et al. [3]	0.61 (0.43)	0.75 (0.10)	0.20 (0.10)	–	–	–
Side vessels	FC-HLSE	0.24 (0.13)	**0.90(0.04)**	0.06 (0.04)	**0.50(0.45)**	**0.86(0.12)**	**0.13(0.17)**
	Hammouche et al. [10]	0.25 (0.12)	0.88 (0.05)	**0.05(0.04)**	–	–	–
	Kermani et al. [14]	0.34 (0.32)	0.85 (0.08)	0.11 (0.09)	0.77 (0.46)	0.77 (0.12)	0.16 (0.13)
	Faraji et al. [21]	0.24 (0.11)	0.87 (0.05)	0.06 (0.05)	0.74 (0.18)	0.73 (0.60)	0.21 (0.18)
	Yang et al. [20]	**0.23(0.12)**	0.90 (0.04)	–	0.59 (0.49)	0.83 (0.14)	–
	Mendizabal et al. [15]	0.38 (0.19)	0.84 (0.07)	0.11 (0.11)	–	–	–
	Wang et al. [3]	0.59 (0.23)	0.80 (0.10)	0.16 (0.13)	–	–	–
	Alberti et al. [3]	0.47 (0.24)	0.79 (0.07)	0.17 (0.09)	–	–	–
Shadow	FC-HLSE	0.28 (0.19)	**0.89(0.06)**	0.07 (0.06)	**0.59(0.47)**	**0.82(0.15)**	0.16 (0.19)
	Hammouche et al. [10]	0.28 (0.13)	0.86 (0.07)	**0.06(0.06)**	–	–	–
	Kermani et al. [14]	0.36 (0.22)	0.83 (0.07)	0.11 (0.07)	1.01 (0.39)	0.72 (0.12)	**0.12(0.13)**
	Faraji et al. [21]	0.29 (0.20)	0.86 (0.07)	0.08 (0.09)	1.24 (0.39)	0.58 (0.13)	0.37 (0.15)
	Yang et al. [20]	**0.27(0.25)**	0.87 (0.06)	–	0.80 (0.45)	0.76 (0.12)	–
	Mendizabal et al. [15]	0.43 (0.27)	0.83 (0.09)	0.12 (0.11)	–	–	–
	Wang et al. [3]	0.59 (0.27)	0.81 (0.10)	0.18 (0.16)	–	–	–
	Alberti et al. [3]	0.53 (0.29)	0.78 (0.08)	0.18 (0.09)	–	–	–

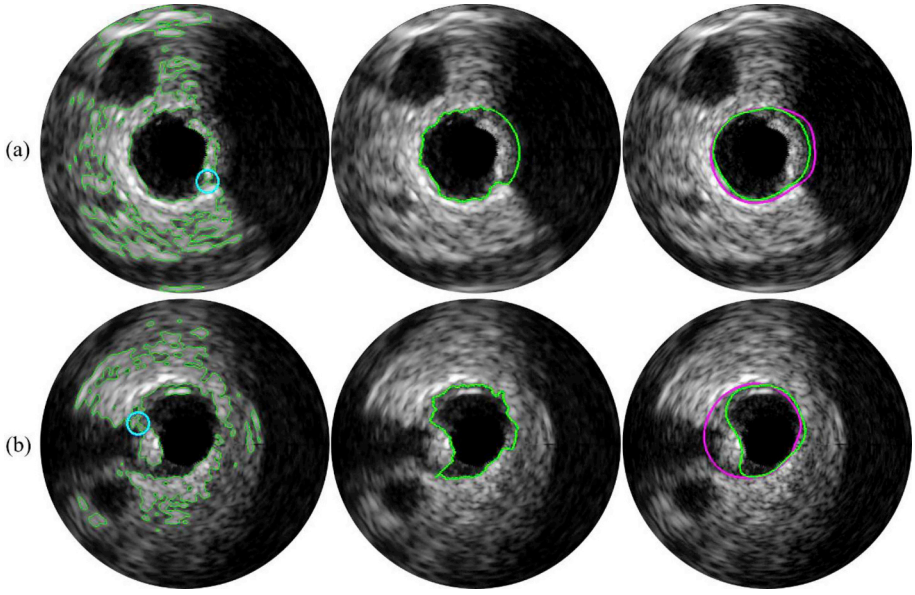

Fig. 9. An example of (a) accurate and (b) inaccurate result after the 1st round LSE (first column), the contour extraction and refinement (second column), and the 2nd round LSE (third column) for the MA border detection. The magenta contour corresponds to the ground truth.

Table 5
Details about the proposed FC-HLSE and other published methods.

	Category	Semi/auto	Hardware used	2D/3D	Time per frame (s)
FC-HLSE	Lumen and media	auto	Xeon E5-2637 3.5 GHz	2D	7.31 ± 2.14
Hammouche et al. [10]	Lumen	auto	Core i7-4500U, 1.8 GHz	3D	0.07
Kermani et al. [14]	Lumen and media	auto	–	2D	–
Faraji et al. [21]	Lumen and media	auto	Core i7-4700HQ, 2.4 GHz	2D	0.19
Yang et al. [20]	Lumen and media	auto	Core i7-8700K	2D	0.15
Jodas et al. [24]	Lumen	auto	Core i7-4700HQ, 2.4 GHz	2D	5.72 ± 1.54
Lo Vercio et al. [8]	Lumen	auto	Core i7-3630QM, 2.4 GHz	2D	1.27–4.59
Mendizabal et al. [15]	Lumen	semi	Core i7, 2 GHz	2D	4.96
Wang et al. [3]	Lumen	semi	Xeon 2.67 GHz	2D	100
Alberti et al. [3]	Lumen	semi	Core 2, Duo 2.13 GHz	3D	13

Acknowledgment

This work is supported by National Key Research and Development Program of China (No.2018YFC0116303).

References

[1] J. Frostegard, SLE, atherosclerosis and cardiovascular disease, J. Intern. Med. 257 (2005) 485–495 https://doi.org/10.1111/j.1365-2796.2005.01502.x.
[2] A. Katouzian, E.D. Angelini, S.G. Carlier, J.S. Suri, N. Navab, A.F. Laine, A state-of-the-art review on segmentation algorithms in intravascular ultrasound (IVUS) images, IEEE Trans. Inf. Technol. Biomed. 16 (2012) 823–834 https://doi.org/10.1109/TITB.2012.2189408.
[3] S. Balocco, C. Gatta, F. Ciompi, A. Wahle, P. Radeva, S. Carlier, G. Unal, E. Sanidas, J. Mauri, X. Carillo, T. Kovarnik, C.-W. Wang, H.-C. Chen, T.P. Exarchos, D.I. Fotiadis, F. Destrempes, G. Cloutier, O. Pujol, M. Alberti, E.G. Mendizabal-Ruiz, M. Rivera, T. Aksoy, R.W. Downe, I.A. Kakadiaris, Standardized evaluation methodology and reference database for evaluating IVUS image segmentation, Comput. Med. Imag. Graph. 38 (2014) 70–90 https://doi.org/10.1016/j.compmedimag.2013.07.001.
[4] F.S. Zakeri, S.K. Setarehdan, S. Norouzi, Automatic media-adventitia IVUS image segmentation based on sparse representation framework and dynamic directional active contour model, Comput. Biol. Med. 89 (2017) 561–572 https://doi.org/10.1016/j.compbiomed.2017.03.022.
[5] Y. Wang, W. Peng, C. Qiu, J. Jiang, S. Xia, Fractional-order Darwinian PSO-based feature selection for media-adventitia border detection in intravascular ultrasound images, Ultrasonics 92 (2019) 1–7 https://doi.org/10.1016/j.ultras.2018.06.012.
[6] F. Chen, R. Ma, J. Liu, M. Zhu, H. Liao, Lumen and media-adventitia border detection in IVUS images using texture enhanced deformable model, Comput. Med. Imag. Graph. 66 (2018) 1–13 https://doi.org/10.1016/j.compmedimag.2018.02.003.
[7] J.H. Lee, Y.N. Hwang, G.Y. Kim, K.S. Min, Segmentation of the lumen and media adventitial borders in intravascular ultrasound images using a geometric deformable model, IET Image Process. 12 (2018) 1881–1891 https://doi.org/10.1049/iet-ipr.2017.1143.
[8] L. Lo Vercio, J.I. Orlando, M. del Fresno, I. Larrabide, Assessment of image features for vessel wall segmentation in intravascular ultrasound images, Int. J. Comput. Assist. Radiol. Surg. 11 (2016) 1397–1407 https://doi.org/10.1007/s11548-015-1345-4.
[9] A. Hammouche, G. Cloutier, J. Tardif, J. Meunier, Space curve approach for IVUS image segmentation, IEEE Life Sci. Conf. (2018) 37–40 https://doi.org/10.1109/lsc.2018.8572073.
[10] A. Hammouche, G. Cloutier, J.C. Tardif, K. Hammouche, J. Meunier, Automatic IVUS lumen segmentation using a 3D adaptive helix model, Comput. Biol. Med. 107 (2019) 58–72 https://doi.org/10.1016/j.compbiomed.2019.01.023.
[11] M.H.R. Cardinal, G. Soulez, J.C. Tardif, J. Meunier, G. Cloutier, Fast-marching segmentation of three-dimensional intravascular ultrasound images: a pre- and post-intervention study, Med. Phys. 37 (2010) 3633–3647 https://doi.org/10.1118/1.3438476.
[12] F. Destrempes, M.H. Roy Cardinal, L. Allard, J.C. Tardif, G. Cloutier, Segmentation method of intravascular ultrasound images of human coronary arteries, Comput. Med. Imag. Graph. 38 (2014) 91–103 https://doi.org/10.1016/j.compmedimag.2013.09.004.
[13] J. Yan, D. Lv, Y. Cui, A novel segmentation approach for intravascular ultrasound images, J. Med. Biol. Eng. 37 (2017) 386–394 https://doi.org/10.1007/s40846-017-0233-5.
[14] A. Ayatollahi Kermani, A new nonparametric statistical approach to detect lumen and Media-Adventitia borders in intravascular ultrasound frames, Comput. Biol. Med. 104 (2019) 10–28 https://doi.org/10.1016/j.compbiomed.2018.10.024.
[15] E.G. Mendizabal-Ruiz, G. Biros, I.A. Kakadiaris, Segmentation of the luminal border in intravascular ultrasound using a physics-based scattering model and inverse problem approach, Med. Image Anal. 17 (2013) 649–670 https://doi.org/10.1016/j.media.2013.02.003.
[16] F. Ciompi, O. Pujol, C. Gatta, M. Alberti, S. Balocco, X. Carrillo, J. Mauri-Ferre, P. Radeva, HoliMAb: a holistic approach for Media-Adventitia border detection in intravascular ultrasound, Med. Image Anal. 16 (2012) 1085–1100 https://doi.org/10.1016/j.media.2012.06.008.
[17] E. Essa, X. Xie, Automatic segmentation of cross-sectional coronary arterial images, Comput. Vis. Image Understand. 165 (2017) 97–110 https://doi.org/10.1016/j.cviu.2017.11.004.
[18] S. Tsantis, G.C. Kagadis, K. Katsanos, D. Karnabatidis, G. Bourantas, G.C. Nikiforidis, Automatic vessel lumen segmentation and stent strut detection in intravascular optical coherence tomography, Med. Phys. 39 (2012) 503–513 https://doi.org/10.1118/1.3673067.
[19] S. Su, Z. Hu, Q. Lin, W.K. Hau, Z. Gao, H. Zhang, An artificial neural network method for lumen and media-adventitia border detection in IVUS, Comput. Med. Imag. Graph. 57 (2017) 29–39 https://doi.org/10.1016/j.compmedimag.2016.11.003.
[20] J. Yang, L. Tong, M. Faraji, A. Basu, IVUS-Net, An intravascular ultrasound segmentation network, Int. Conf. Smart Multimed (2018) 367–377 https://arxiv.org/abs/1806.03583.
[21] M. Faraji, I. Cheng, I. Naudin, A. Basu, Segmentation of arterial walls in intravascular ultrasound cross- sectional images using extremal region selection, Ultrasonics 84 (2018) 356–365 https://doi.org/10.1016/j.ultras.2017.11.020.
[22] Z. Gao, W.K. Hau, M. Lu, W. Huang, H. Zhang, W. Wu, X. Liu, Y.T. Zhang, Automated framework for detecting lumen and media-adventitia borders in intravascular ultrasound images, Ultrasound Med. Biol. 41 (2015) 2001–2021 https://doi.org/10.1016/j.ultrasmedbio.2015.03.022.
[23] Od Wong, A. Rodtook, S. Rasmequan, K. Chinnasarn, Automated segmentation of media-adventitia and lumen from intravascular ultrasound images using non-parametric thresholding, 9th Int. Conf. Knowl. Smart Technol. (2017) 220–225 https://doi.org/10.1109/KST.2017.7886110.
[24] D.S. Jodas, A.S. Pereira, J.M.R.S. Tavares, Automatic segmentation of the lumen region in intravascular images of the coronary artery, Med. Image Anal. 40 (2017) 60–79 https://doi.org/10.1016/j.media.2017.06.006.
[25] K.S. Chuang, H.L. Tzeng, S. Chen, J. Wu, T.J. Chen, Fuzzy c-means clustering with spatial information for image segmentation, Comput. Med. Imag. Graph. 30 (2006) 9–15 https://doi.org/10.1016/j.compmedimag.2005.10.001.
[26] R. Rahmat, D. Harris-Birtill, Comparison of level set models in image segmentation, IET Image Process. 12 (2018) 2212–2221 https://doi.org/10.1049/iet-ipr.2018.5796.
[27] T.F. Chan, L.A. Vese, Active contours without edges, IEEE Trans. Image Process. 10 (2001) 266–277 https://doi.org/10.1109/83.902291.
[28] C. Li, C. Xu, C. Gui, M.D. Fox, Distance regularized level set evolution and its application to image segmentation, IEEE Trans. Image Process. 19 (2010) 3243–3254 https://doi.org/10.1109/TIP.2010.2069690.
[29] O. Kubler, R. Kikinis, F.A. Jolesz, Nonlinear anisotropic filtering of MRI data, IEEE Trans. Med. Imaging 11 (1992) 221–232 https://doi.org/10.1109/42.141646.
[30] B.N. Li, C.K. Chui, Integrating spatial fuzzy clustering with level set methods for automated medical image segmentation, Comput. Biol. Med. 41 (2011) 1–10 https://doi.org/10.1016/j.compbiomed.2010.10.007.
[31] B.N. Li, J. Qin, R. Wang, M. Wang, X. Li, Selective level set segmentation using fuzzy region competition, IEEE Access 4 (2016) 4777–4788 https://doi.org/10.1109/ACCESS.2016.2590440.
[32] V. Pratt, Direct least-squares fitting of algebraic surfaces, ACM SIGGRAPH Comput. Graph, ACM, 1987, pp. 145–152 https://doi.org/10.1145/37401.37420.